EXPERIMENTAL AND NUMERICAL ANALYSIS ON THE TENSILE-BEARING CAPACITY OF AN INNOVATIVE OFFSHORE FLOATING PHOTOVOLTAIC PLATFORM CONNECTOR

Zhi-Yong Zheng [1, 2], Hong-Bo Liu [1, 3, *], Liu-Lu Guo [3], Ji-Jian Lian [3], Xiang-Yu Yan [4] and Ye Yao [4]

[1] School of Water Conservancy and Hydroelectric Power, Hebei University of Engineering, Handan 056000, China

[2] Hebei Institute of Mechanical and Electrical Technology, Xingtai 054000, China

[3] Department of Civil Engineering, Tianjin University, Tianjin 300072, China

[4] School of Ocean Energy, Tianjin University of Technology, Tianjin 300384, China

* (Corresponding author: E-mail: hbliu@tju.edu.cn)

A B S T R A C T

Offshore floating photovoltaic (OFPV) systems have attracted considerable attention from the scientific community because of their broad application prospects. A multi-module configuration interconnected via connectors is typically used in OFPV platforms. The tensile-bearing capacity of the connectors is crucial to ensure the overall safety of OFPV platforms. In this study, the tensile-bearing capacity of an innovative connector was investigated by experiments and numerical simulations. The numerical simulation results conformed well with those from experiments, with a relative error of less than 10%. Subsequently, The tensile mechanism of the connectors was analyzed, leading to the derivation of equations used to determine the tensile-bearing capacity of the OFPV platform connector under two distinct failure modes. Finally, a parametric study was conducted to elucidate the relationship between the tensile-bearing capacity of the connectors and the connecting pipe and baseplate thicknesses. The results obtained from the derived equations agreed well with those from numerical simulations, indicating that the equations could be used to determine the tensile-bearing capacity of OFPV platform connectors. This study lays the theoretical foundation for the design and application of OFPV structures.

1.   Introduction

The power generation efficiency has been increased by about 5% on average due to the cooling effect caused by contact with seawater [1, 2]. Therefore, OFPV technology has garnered much interest from scholars and experts to optimize the utilization of marine resources and solar energy [3]. This technology primarily involves photovoltaic devices, support structures, and anchoring systems [4, 5].   Although floating photovoltaic technology has reached a relatively mature stage for inland water systems, the harsh marine environment characterized by strong winds and waves as well as corrosive conditions of the saline water poses significant challenges to the large-scale development and deployment of OFPV systems in oceanic settings [6-8]. Multi-module OFPV platforms interconnected via connectors have been developed to address the challenges presented by complex marine environments. In practical applications, this configuration typically consists of hundreds or even thousands of modules and connectors that can interact with significant forces [9, 10]. Thus, the reliability of these connectors is crucial to ensure the overall safety of OFPV platforms, necessitating an exceptionally

high load-bearing capacity for the connectors [11]. Currently, The main forms of connectors include: hinged connectors [12-16], chain connections [17-19] and rigid connections [20]. The most widely used type of the connector is the hinged connector. However, the hinged connector restricts too many degrees of freedom[21, 22], only allowing adjacent OFPV platforms to rotate at a certain angle relative to each other, which seriously affects the wave-following performance of the structure. The chain connection releases most degrees of freedom between adjacent OFPV platforms. However, under the action of wave loads, the adjacent platforms might experience severe collisions, which greatly affect the safety of the platform structure. Rigid connection completely restricts the degrees of freedom between adjacent OFPV platforms[23], making the wave-following performance of the structure even worse. Moreover, under the action of wave loads, significant bending moments might be generated at the connectors, which makes this area highly prone to fracture and damage. Meanwhile, many experts [24-31] have conducted in-depth studies on the hydrodynamic responses of multi-module OFPV platforms at different connectors.
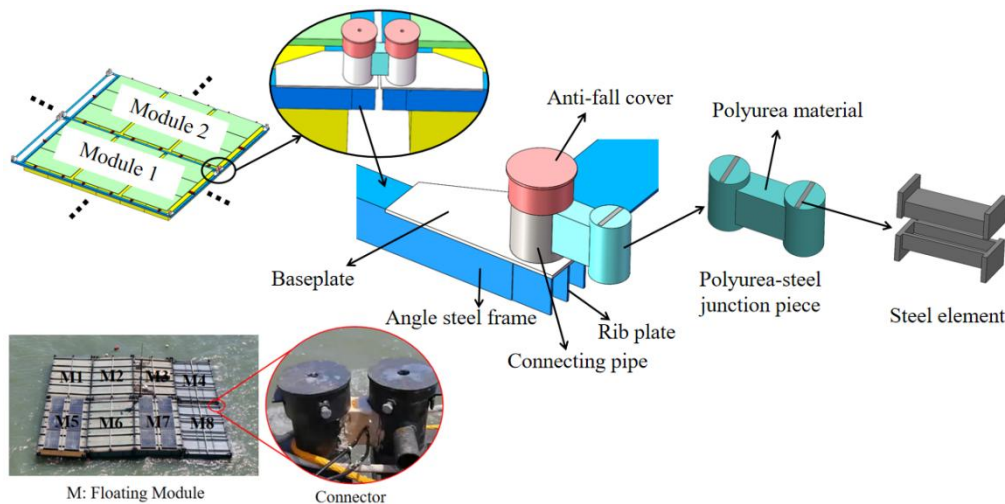

Fig. 1 The configuration of the connector

This paper presents an Innovative connector of the OFPV Platforms, which primarily comprises four components: a baseplate, a connecting pipe, an anti-fall cover, and a polyurea–steel junction component. The configuration of the connector is illustrated in Fig. 1. This connector combines the advantages of most connection forms. Compared with the hinged connector and the rigid connection, this connector releases more degrees of freedom for the OFPV platform and has better wave-following performance. Meanwhile, compared with the chain connection, this connector can not only bear the equivalent tensile force but also have higher impact resistance. More importantly, due to the application of polyurea material, it has higher durability in the marine corrosion environment.

Based on the literature survey, Most of the studies are focused on the hydrodynamic and hydroelastic responses of floating photovoltaic platforms with multiple modules. However, there is a paucity of studies on the mechanical properties of the connectors of the OFPV platforms. According to the research findings of experts, The mechanical properties of the connectors are crucial to ensure the safety of the entire structure[21-23, 32-34]. Accurately determining the tensile-bearing capacity of the connectors not only enhances the design of OFPV platforms but also facilitates the safety assessment of OFPV platforms. This paper presents an in-depth investigation into the tensile performance of this innovative connector utilized in OFPV platforms and introduces a method for calculating the tensile-bearing capacity.

2. Experimental study

2.1. Design of the test specimens

Eighteen test specimens were designed and fabricated for tensile tests using Q235B steel. The variables investigated were the connecting pipe thickness (d = 8, 14, and 20 mm) and baseplate thickness (t = 0, 9 , and 14 mm). The detailed schematic of the specimen is shown in Fig. 2. The variables investigated are presented in Table 1. In this table, 'C' represents 'Connector,' and the first and second digits represent the thicknesses of the connecting pipe and baseplate, respectively. To ensure the reliability of the experimental results, two specimens (designated A and B) were prepared for each group.

Table 1
Details of the test specimens

Notation	d（mm）	t (mm)	Notation	d（mm）	t (mm)
C-8-0	8	0	C-14-14	14	14
C-8-9	8	9	C-20-0	20	0
C-8-14	8	14	C-20-9	20	9
C-14-0	14	0	C-20-14	20	14
C-14-9	14	9			

Fig. 2 The detailed schematic of the specimen

(a) diagram

(b) physical drawing

Fig. 3 The experimental setup

2.2. Experimental setup

The experimental setup is shown in Fig. 3. One end of the specimen was fastened to the supporting frame using a connection plate, and the opposite end was connected to a specialized jack interface via a polyurea–steel junction component. The inner diameter of the jack interface matched that of the connecting pipe of the test specimen, whereas its thickness was significantly increased to ensure structural integrity during testing. The hydraulic jack was capable of exerting a force of 50 kN, and a load cell was used to precisely measure the applied force.

The loading procedure was divided into two distinct phases: preloading and formal loading. The preloading phase was conducted to minimize measurement errors that could arise from gaps between the specimen and the loading device. Following this, the formal loading phase involved displacement-controlled loading at a rate of 2 mm/min until the specimen failed or the real-time load decreased to 80% of its peak value.

2.3. Layout of the measurement points

The layout of the displacement and strain measurement points during the experiment is shown in Fig. 4. Linear variable differential transformers (DM1) were installed to measure the displacement along the direction of the applied force. Ten strain gauges were employed to assess the strain at critical locations on the test specimen. Six of these gauges (SG1–SG6) were strategically positioned along the half-circumference of the connecting pipe, specifically at the middle and lower heights of the opening, to monitor the strains within the connecting pipe. In addition, two strain gauges (SG7 and SG8) were affixed on the rear and lateral surfaces of the baseplate to evaluate the strain response. Two strain gauges (SG9 and SG10) were installed on the underside and rear side of the angle steel frame to measure the strains at these locations.
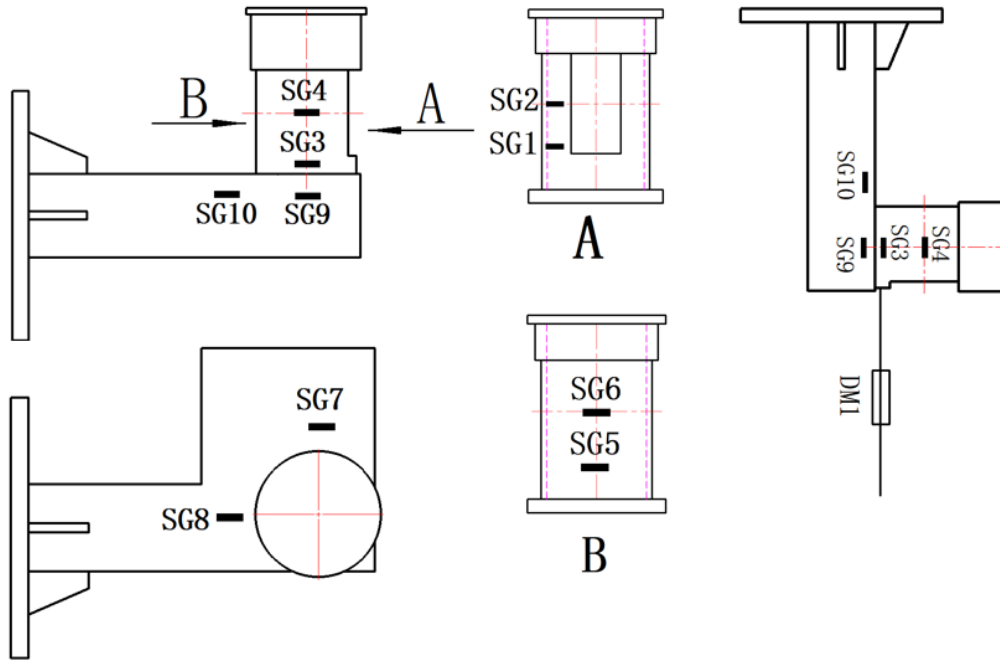
Fig. 4 Schematic diagram of strain gauge and displacement meter arrangement

3. Experimental results

3.1. Failure modes

As shown in Fig. 5, the test specimen exhibited two distinct failure modes: bulging deformation at the opening of the connecting pipe and buckling deformation of the angle steel frame. The two failure modes do not act independently. Their combined effect influences the tensile-bearing capacity of connectors. Additionally, when the connecting pipe fails due to bulging, the angle steel frame undergoes a certain degree of buckling deformation, though it does not yet reach the point of failure, and vice versa. Consequently, two failure modes collectively impact the tensile-bearing capacity of the connectors.

When the connecting pipe thickness was $d = 8$ mm, the failure mode observed in the test specimen manifested as localized bulging deformation at the opening of the connecting pipe. As the tensile force reached a critical threshold, localized bulging deformation was initiated at this opening, significantly increasing the risk of detachment of the polyurea–steel junction component from the connecting pipe. At this point, the opening of the connecting pipe reached its ultimate strength, leading to a corresponding decrease in the load-bearing capacity of the test specimen.
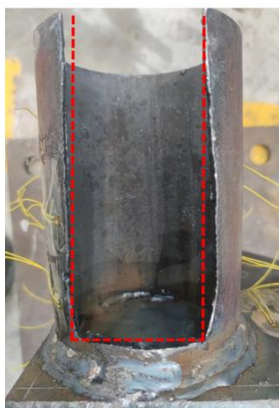
(a) The opening of connecting pipe has exhibited bulging deformation

(b) The angle steel frame has exhibited buckling deformation

Fig. 5 Failure modes of specimen

When the connecting pipe thickness was d = 14 mm, the test specimen exhibited two distinct failure modes: localized bulging deformation at the opening of the connecting pipe and buckling deformation of the angle steel frame. When the baseplate thicknesses were t = 0 and 14 mm, the angle steel frame near the base of the connecting pipe began to deform into folds when subjected to a certain level of tensile force. Subsequently, a significant decrease in the load-bearing capacity of the test specimen was observed. When the baseplate thickness was t = 9 mm, bulging occurred at the opening of the connecting pipe upon reaching a specific tensile force threshold, after which a significant reduction in the tensile-bearing capacity was observed.

When the connecting pipe thickness was d = 20 mm, the failure mode observed in the test specimen was characterized by severe buckling deformation of the angle steel frame adjacent to the connecting pipe. As the tensile force reached a critical threshold, severe buckling deformation was initiated in the angle steel frame located near the bottom of the connecting pipe, resulting in a corresponding decline in the tensile-bearing capacity of the test specimen.

3.2. Load-displacement curves
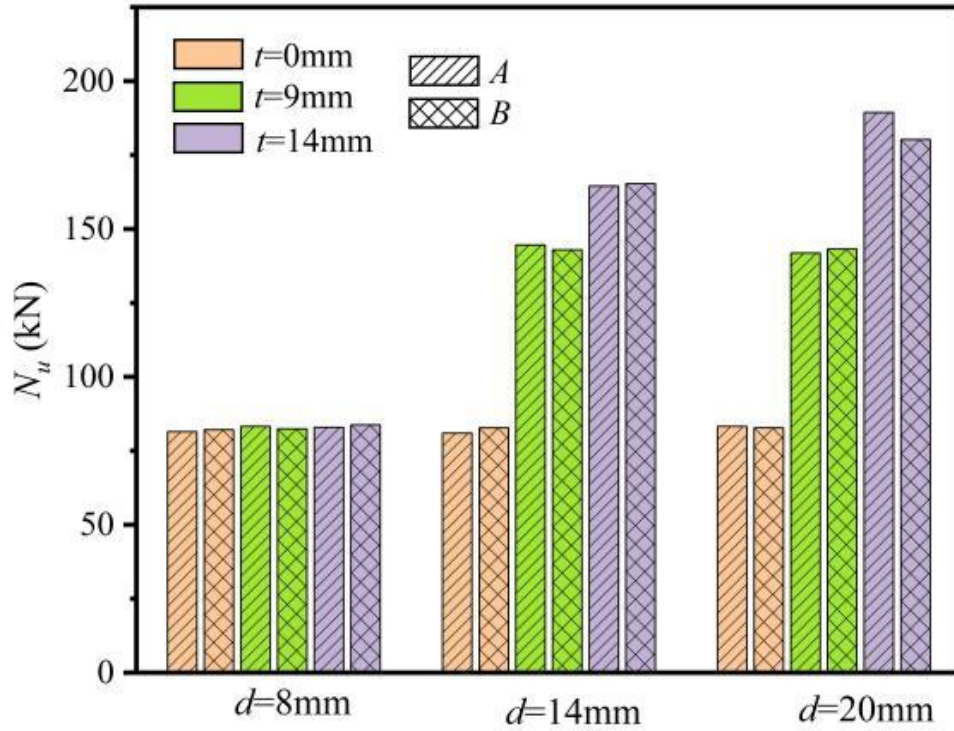
Fig. 6 The column chart of the bearing capacity of the specimen

a. d = 8 mm　　　　　　　　b. d = 14 mm　　　　　　　　c. d = 20 mm
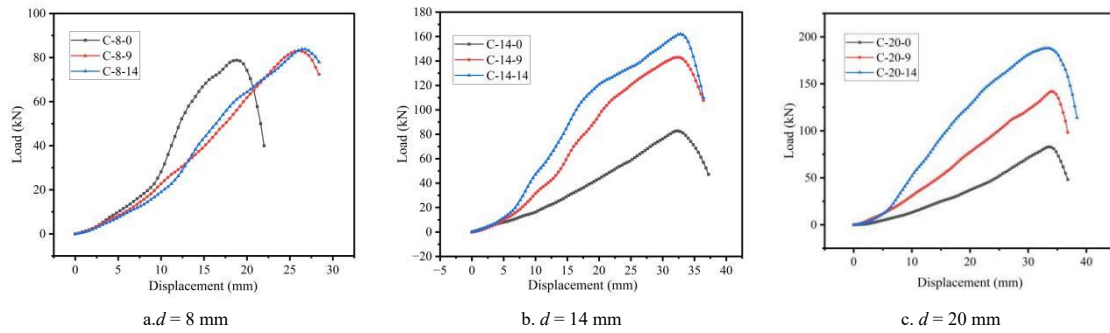
Fig. 7 Load-displacement curve of specimen

Table 2
The maximum bearing capacity and failure mode of the specimen

Notation	N_{uTEST} (kN)	Failure mode	Notation	N_{uTEST} (kN)	Failure mode
C-8-0A	81.46	D	C-14-9B	142.89	F
C-8-0B	82.07	D	C-14-14A	164.47	D
C-8-9A	83.25	D	C-14-14B	165.23	D
C-8-9B	82.42	D	C-20-0A	83.21	F
C-8-14A	82.89	D	C-20-0B	82.69	F
C-8-14B	83.75	D	C-20-9A	141.82	F
C-14-0A	80.94	F	C-20-9B	143.15	F
C-14-0B	82.74	F	C-20-14A	189.34	F
C-14-9A	144.56	F	C-20-14B	180.21	F

Note: N_{uTEST} is the maximum tensile-bearing capacity of the specimen ascertained from experiments, D is the bulging deformation of the connecting pipe opening, and F is the buckling deformation of the angle steel frame.

The maximum tensile-bearing capacity (N_u) results and load-displacement curves for all test specimens are presented in Fig. 6 and Fig. 7, respectively. The detailed results are summarized in Table 2. It is evident that the tensile-bearing capacity of the test specimens was influenced by the combined effects of the connecting pipe and baseplate thicknesses. Specifically, when d = 8 mm, changes in the baseplate thickness had minimal effect on the tensile-bearing capacity. Conversely, when d = 14 and 20 mm, an increase in the baseplate thickness enhanced the tensile-bearing capacity. Similarly, when t = 0 mm, changes in the connecting pipe thickness had only a minor effect on the tensile-bearing capacity. In contrast, when t = 9 and 14 mm, a higher connecting pipe thickness resulted in a higher tensile-bearing capacity.

3.3. Load-strain curves

Based on the experimental results, the strain measurements at SG4 and SG10 of the test specimens exhibited greater significance. The load–strain curves for all test specimens measured at SG4 and SG10 are shown in Fig. 8 to Fig. 10. It is apparent that the connecting pipe thickness had a pronounced effect on the strains measured at these locations. At SG4 under the same loading conditions, an increase in the connecting pipe thickness resulted in higher strain. Conversely, at SG10 under the same loading conditions, a decrease in the connecting pipe thickness resulted in a higher strain, where the maximum strain was observed when d = 8 mm, which far exceeded those observed when d = 14 and 20 mm. The baseplate thickness also had a considerable effect on the strains measured at SG10. During the initial loading phase, all of the test specimens exhibited similar trends in their strains at this location. However, as the load further increased, the test specimens with thicker baseplates exhibited comparatively higher strains.
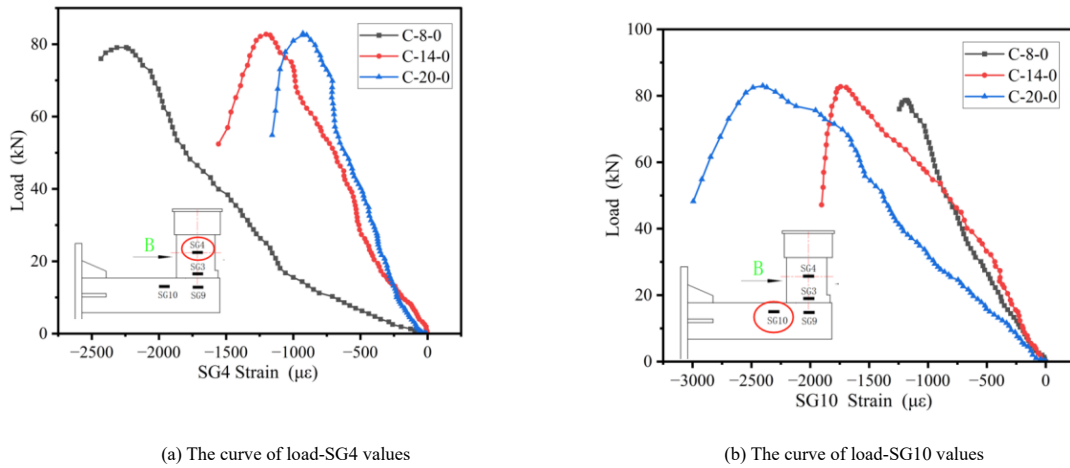

(a) The curve of load-SG4 values   (b) The curve of load-SG10 values

Fig. 8 The load-strain curve at the typical position of the specimen when t=0 mm

(a) The curve of load-SG4 values   (b) The curve of load-SG10 values
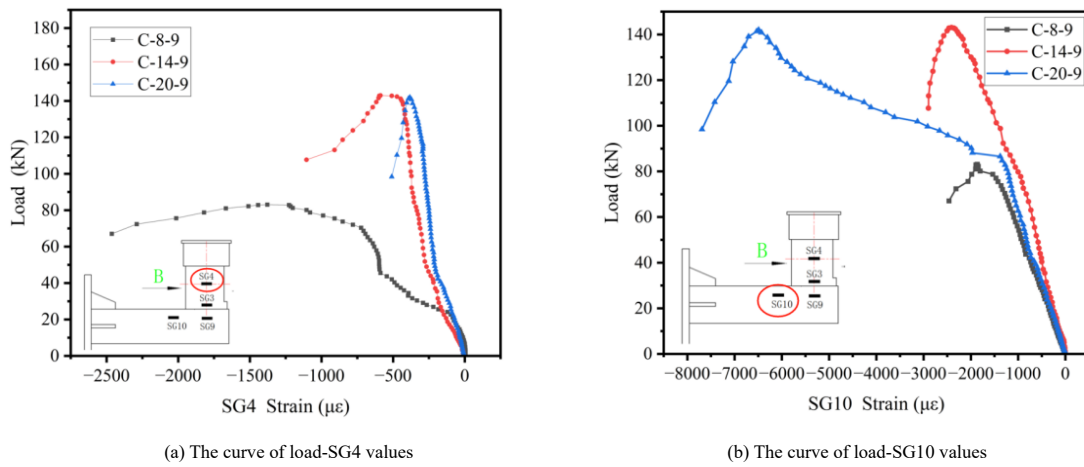
Fig. 9 The load-strain curve at the typical position of the specimen when t=9mm

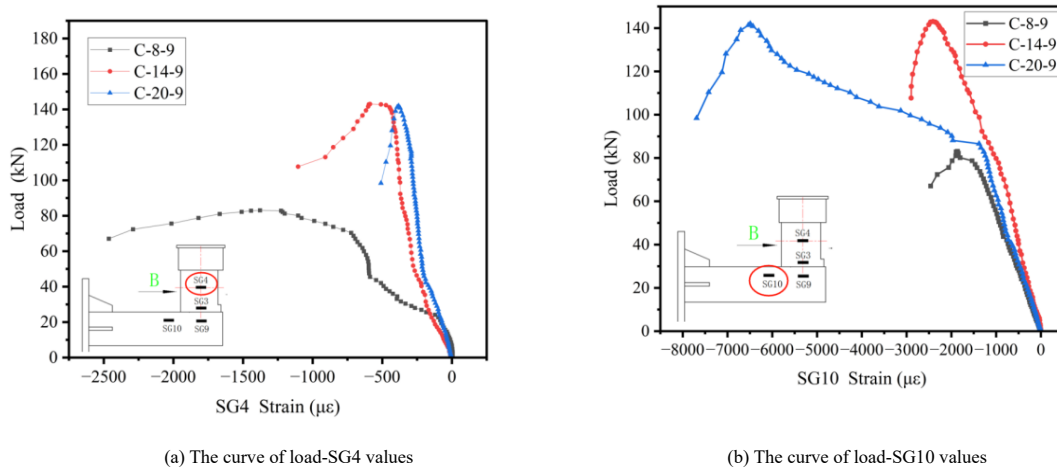(a) The curve of load-SG4 values   (b) The curve of load-SG10 values

Fig. 10 The load-strain curve at the typical position of the specimen when t=14mm

4. Tension mechanism

4.1. Load analysis of the connecting pipe

Neglecting the constraining influence of the angle steel frame at the base of the connecting pipe, this analysis focuses solely on calculating the tensile-bearing capacity of the side-opening connecting pipe. Consider a minute horizontal cross-section at a specified height within the connecting pipe, as shown in Fig. 11(a). The corresponding force distribution is shown in Fig. 11(b). Following the calculations, the bending moment diagram for this cross-section is presented in Fig. 16(c). It is evident that the outer surface of the connecting pipe experienced compression, which was consistent with the compressive strains measured at locations SG1–SG6 in the experiments. The maximum bending moment is calculated by using Eq. 1.

$$dM_{max} = \frac{dF}{2\cos\theta}\left[R\sin(\theta-\alpha)+R+\frac{d}{2}\right] \quad (1)$$

Where, Z is the height of the connecting pipe, $\alpha = \arcsin\dfrac{P}{2R}$, $\theta = \arcsin\dfrac{P}{2r}$, $dF = \dfrac{F}{Z}dz$.

The peak stress is observed at the location of the maximum bending moment and this peak stress is determined using Eq. 2.

$$\sigma_{max} = \frac{dM_a}{W} = \frac{6dM_{max}}{d^2 dz} \quad (2)$$

where, W is the section modulus in bending, which is a measure of the capacity of the material to resist bending.

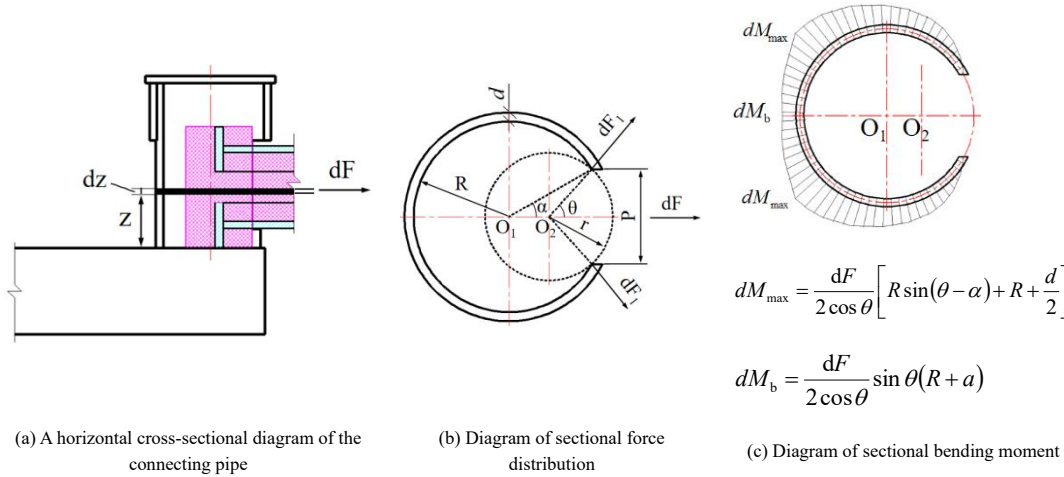The maximum stress can be calculated using Eq.3 by combining Eq.1 and Eq.2.

$$\sigma_{max} = \frac{F}{d^2}\cdot\frac{3\left[R\sin(\theta-\alpha)+R+\dfrac{d}{2}\right]}{\cos\theta} \leq \sigma_s \quad (3)$$

where, σ_s is the yield strength of the materials.

Based on Eq. 3, the tensile-bearing capacity of the connectors under bulging deformation at the opening of the connecting pipe opening is calculated using Eq. 4.

$$N_{uFOR} = F \leq \frac{d^2\sigma_s\cos\theta}{3\left[R\sin(\theta-\alpha)+R+\dfrac{d}{2}\right]} \quad (4)$$

where N_{uFOR} is the tensile-bearing capacity of the connectors under bulging deformation at the opening of the connecting pipe.

These equations fail to account for the constraining effect of the angle steel frame on the base of the connecting pipe. Consequently, the tensile-bearing capacity of the connectors calculated using Eq. 4 is inadequate, and hence, it is necessary to revise the equation. In addition, considering that the magnitude of $R\sin(\theta-\alpha)$ is notably smaller than R, $R\sin(\theta-\alpha)$ may be omitted from Eq. 4. After applying the correction, the tensile-bearing capacity of the connectors is determined using Eq. 5.

$$N_{uC-FOR} = F \leq \frac{d^2\sigma_s\cos\theta}{3\left(R+\dfrac{d}{2}\right)} \quad (5)$$

where NuC-FOR is the corrected tensile-bearing capacity of the connectors under bulging deformation at the opening of the connecting pipe.

Both Eq. 4 and Eq. 5 indicate that the connecting pipe thickness (d) has a significant effect on the tensile-bearing capacity of the connectors. In particular, an increase in d is associated with a decrease in stress and an increase in the tensile-bearing capacity, which is consistent with the experimental observations.

(a) A horizontal cross-sectional diagram of the connecting pipe

(b) Diagram of sectional force distribution

(c) Diagram of sectional bending moment

$$dM_{max} = \frac{dF}{2\cos\theta}\left[R\sin(\theta-\alpha)+R+\frac{d}{2}\right]$$

$$dM_b = \frac{dF}{2\cos\theta}\sin\theta(R+a)$$

Fig. 11 Diagram of load analysis for the connecting pipe section

4.2. Force analysis of the angle steel frame

The loading condition at the connector is simplified according to the following procedure, as shown in Fig. 12(a). (1) The effect of the connecting pipe opening on the sectional coefficient is neglected, and the connecting pipe is modeled as a closed pipe. (2) The tensile force is modeled as a uniformly distributed load acting on the connecting pipe. A simplified bending moment diagram for the connector, which is derived from the force analysis, is shown in Fig. 12(b). The maximum bending moment is determined by using Eq. 6.

$$M_{max} = F\left(\frac{l}{2}+h\right) \quad (6)$$

Where, l is the contact height between the polyurea-steel junction component and the connecting pipe. F is he tensile force of the connectors. h is the vertical distance from the centroid of the angle steel, equipped with a baseplate, to the top surface of the baseplate. As shown in Fig. 13. Mmax is the maximum bending moment induced by the tensile force of the connectors to the centroid axis of the angle steel frame with a baseplate.

$$h = \frac{Bt^2 - Cn^2 - n(C-n)}{2\left[Bt+Cn+(C-n)n\right]} \quad (7)$$

Where, B is the width of the baseplate; t is the height of the baseplate; C is the edge length of the angle steel; n is the thickness of the angle steel.

Therefore, the maximum stress of the angle steel frame is determined by using Eq. 8.

$$\sigma = \frac{Mh}{I_z} = \frac{F\left(\dfrac{l}{2}+h\right)h}{I_z} \leq \sigma_s \quad (8)$$

where, σ is the maximum stress of the angle steel frame; σ_s is the yield strength of steel; I_z is the moment of inertia of the angle steel frame with a baseplate.

By integrating Eq.7 and Eq. 8, the tensile-bearing capacity of the connectors under buckling deformation of the angle steel frame is calculated by using Eq 9.

$$N_{uJF} = F \le \frac{\sigma_s I_Z}{\left(\frac{l}{2}+h\right)h} \qquad (9)$$
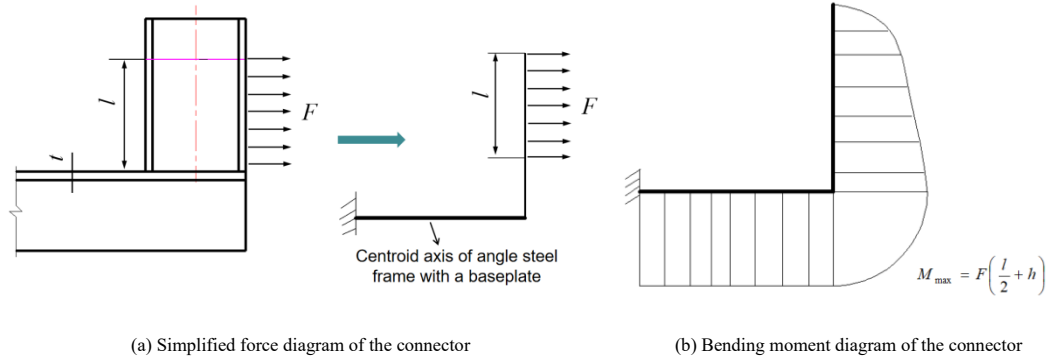
where, N_{uJF} is the tensile-bearing capacity of the connectors determined from the equation applicable for buckling deformation of the angle steel frame.

It is evident from Eq. 8 and Eq. 9 that the baseplate thickness (t) has a substantial effect on the stress distribution within the angle steel frame. An increase in t is associated with a decrease in stress and an improvement in the tensile-bearing capacity of the connectors, which is consistent with the experimental results. As the value of t increased, the stress within the angle steel frame diminished and the tensile-bearing capacity of the connectors increased, both of which agree with the experimental findings.

(a) Simplified force diagram of the connector   (b) Bending moment diagram of the connector

Fig. 12 Simplified force and bending moment diagram of the connector
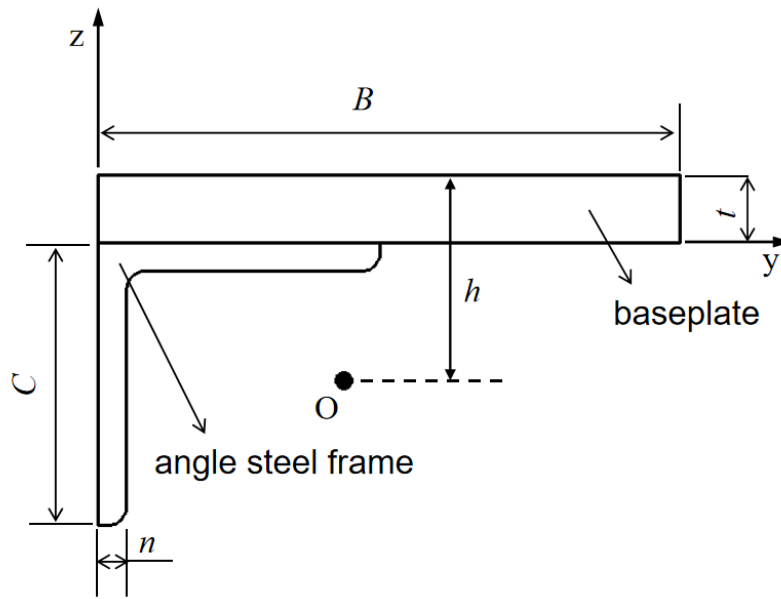
Fig. 13 Section diagram of Angle steel with a baseplate

5. Numerical simulations

5.1. Material properties

Q235B steel was used for the connectors. To determine the properties of the material, tensile tests were conducted following the ISO 6892-1 standard [35], and the properties are tabulated in Table 3. The constitutive model of polyurea is based on the Mooney–Rivlin framework and the specific parameters are listed in Table 4 [36].

Table 3
Average values of the properties of Q235B steel

Materials	E_0 (MPa)	f_y (MPa)	f_u (MPa)	ε_u
Q235B	205700	281.53	432.74	0.22

Note: E_0 is the Young's modulus; f_y is the yield strength of steel; f_u is the ultimate strength, and ε_u is the corresponding tensile strain.

Table 4
Parameters of the Mooney-Rivlin model   Unit: MPa

c_{10}	c_{01}	c_{11}	c_{20}	c_{02}	c_{21}	c_{12}	c_{30}	c_{03}
12.369	8.124	-17.653	7.274	3.062	-0.437	-0.298	0.043	2.94

5.2. Modelling details

The finite element model employs solid elements for simulation, which is comprised of connectors and connection plates. Integrating the polyurea material with the steel elements at a common node treatment to effectively simulate their bonded state as a unified entity. The cylindrical surface of the polyurea-steel junction piece is designed to interface with the inner surface of the connecting pipe, where the latter serves as the contact surface and the former acts as the target surface. The interaction between these surfaces is defined as No Separation contact. A fixed constraint is imposed on the end face of the specimen connection plate, while a tensile displacement is applied to the cylindrical surface of the polyurea-steel junction piece at the opposite end.

5.3. Sensitivity analysis of mesh size

In finite element analysis, the mesh size has a significant effect on the numerical simulation results and computational efficiency. Thus, the effects of mesh size (2, 4, 6, 8, and 10 mm) on the tensile-bearing capacity of the C-8-0 specimen were investigated, and the results are presented in Fig. 14. N_{uFEA} is the maximum tensile-bearing capacity of the test specimen obtained from numerical simulations in Fig. 14. Based on the results, a mesh size of 6 mm was selected to simulate the tensile-bearing capacity of the connectors, since this mesh size achieved a desirable balance between computational efficiency and numerical accuracy.
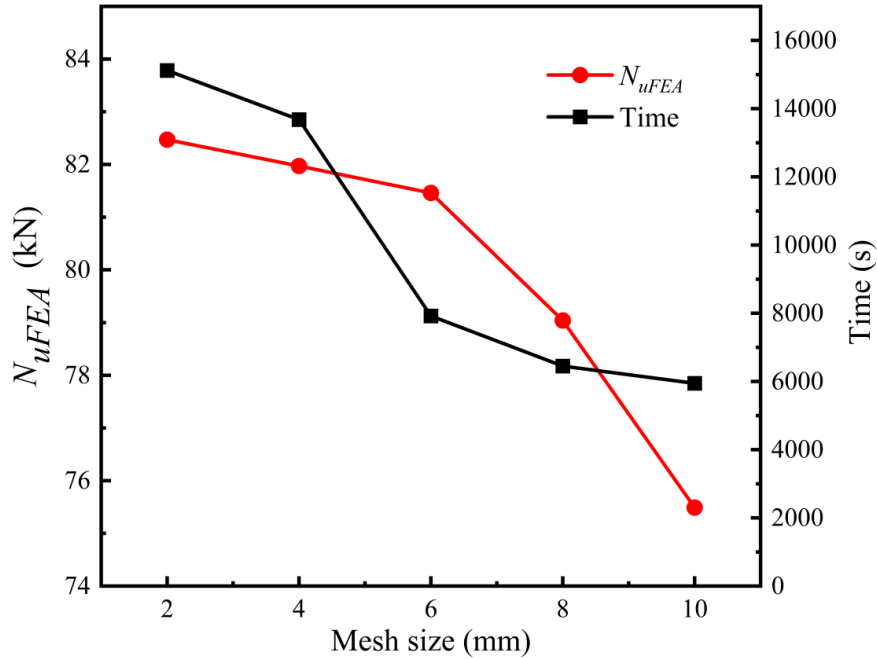
Fig.14 Comparison of simulation efficiency between different mesh sizes

5.4. Validation of the finite element model

The numerical simulation and experimental results for all test specimens were compared, as summarized in Table 5. The relative error between the numerical simulation and experimental results was less than 10%. The failure modes and load-displacement curves of the test specimens are shown in Fig. 14 and Fig. 15, respectively. There was good agreement between the numerical simulation and experimental results, thereby validating that the finite element model was suitable to assess the tensile-bearing capacity of the OFPV platform connector.

Table 5
Comparison between the numerical simulation and experimental results

Notation	N_{uTEST}	N_{uFEA} (kN)	Error	Notation	N_{uTEST}	N_{uFEA} (kN)	Error
C-8-0A	81.46	86.21	5.83%	C-14-9B	142.89	148.36	3.83%
C-8-0B	82.07	86.21	5.04%	C-14-14A	164.47	164.25	0.13%
C-8-9A	83.25	87.24	4.79%	C-14-14B	165.23	164.25	0.59%
C-8-9B	82.42	87.24	5.85%	C-20-0A	83.21	85.68	2.97%
C-8-14A	82.89	86.78	4.69%	C-20-0B	82.69	85.68	3.62%
C-8-14B	83.75	86.78	3.62%	C-20-9A	141.82	149.54	5.44%
C-14-0A	80.94	85.56	5.71%	C-20-9B	143.15	149.52	4.45%
C-14-0B	82.74	85.56	3.41%	C-20-14A	189.34	193.25	2.07%
C-14-9A	144.56	148.36	2.63%	C-20-14B	180.21	193.25	7.24%
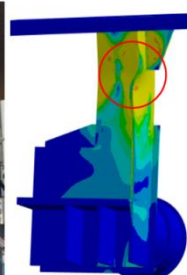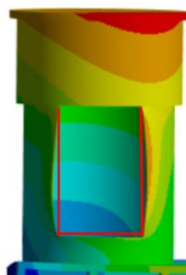
(a) Comparison of bulging deformation of connecting pipe opening   (b) Comparison of buckling deformation in angle steel frame

Fig. 14 Comparison of experimental and finite element analysis results for the failure modes
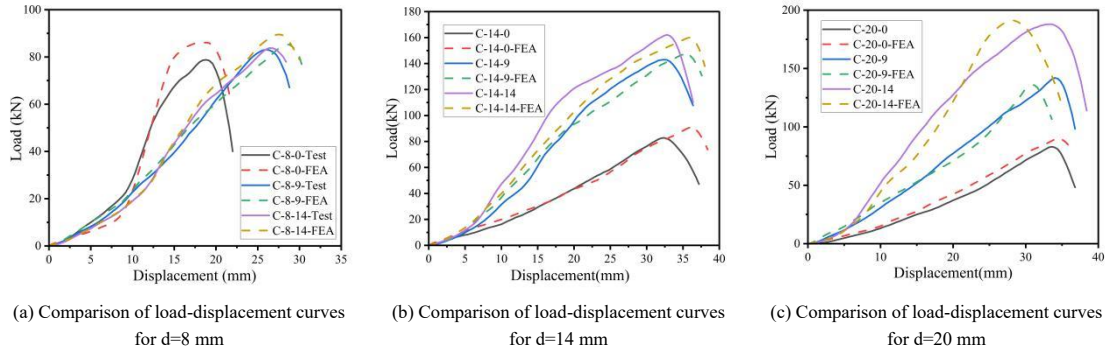
(a) Comparison of load-displacement curves for d=8 mm

(b) Comparison of load-displacement curves for d=14 mm

(c) Comparison of load-displacement curves for d=20 mm

Fig. 15 Comparison of experimental and finite element analysis results for load-displacement curves

5.5. Effect of the connecting pipe thickness

Numerical simulations were conducted using the finite element model to investigate the effect of connecting pipe thickness on the tensile-bearing capacity of the connectors. For simplicity and convenience, the baseplate thickness was set at 0 mm, and the angle steel frame was assumed to remain elastically deformable without yielding or failure. Twenty connecting pipe thicknesses were considered for the numerical simulations, ranging from 1 mm to 20 mm. The tensile-bearing capacities of the connectors for various connecting pipe thicknesses were calculated using Eqs. 4 and 5, and the analytical results were compared with those obtained from numerical simulations. As shown in Fig. 16, the tensile-bearing capacities of the connectors determined using Eq. 4 and Eq. 5 were consistent with those predicted by the finite element model.
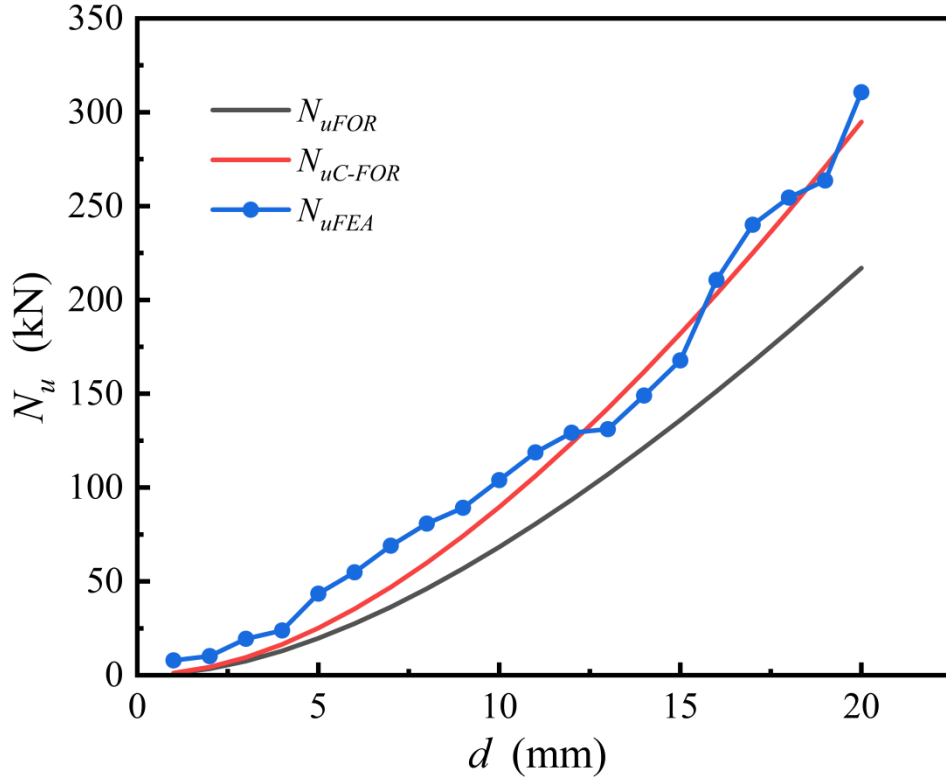

Fig. 16 Comparison of tensile bearing capacity calculated by finite element simulation, Eq.4 and Eq.5

Based on Fig. 16, assuming that the elastic angle steel frame did not yield or fail, the key findings are summarized as follows.

(1) The tensile-bearing capacities of the connectors determined from the unmodified Eq. 4 are substantially lower than those obtained from numerical simulations. This oversight arises from neglecting the effect of the angle steel frame at the bottom of the connecting pipe during the derivation of Eq. 4. With this constraint, the surface stress of the connecting pipe is influenced not only by the horizontal bending moment caused by the connection force acting on the outer side of the connector but also by the vertical bending moment resulting from the connection force applied to the surface of the connector. Hence, the tensile-bearing capacity of the connectors obtained using Eq. 4 is likely to be underestimated.

(2) The tensile-bearing capacities of the connectors obtained using Eq. 5 conform well with those obtained from numerical simulations. In cases where the connecting pipe thickness is minimal, the numerical simulation results surpass the analytical results obtained using Eq. 5. Conversely, in cases where the connecting pipe thickness is substantial, both the numerical simulation and analytical results show excellent agreement, and the trends in the

tensile-bearing capacities were consistent. Thus, it can be deduced that Eq. 5 can be used to accurately assess the tensile-bearing capacity of OFPV platform connectors under bulging deformation of the connecting pipe.

(3) The tensile-bearing capacity of the connectors is directly proportional to the square of the connecting pipe thickness.

5.6. Effect of the baseplate thickness

To investigate the effect of baseplate thickness on the tensile-bearing capacity of the connectors and simplify modeling, the connecting pipe thickness was arbitrarily set at 20 mm, assuming that the connecting pipe would not yield. Twenty-one baseplate thicknesses were considered for the numerical simulations, ranging from 0 mm to 20 mm. The tensile-bearing capacities of the connectors were determined for different baseplate thicknesses using Eq 9 and the values were compared with those predicted by the finite element model, as shown in Fig. 17. The results illustrated the relationship between the baseplate thickness and the tensile-bearing capacity of the connectors.
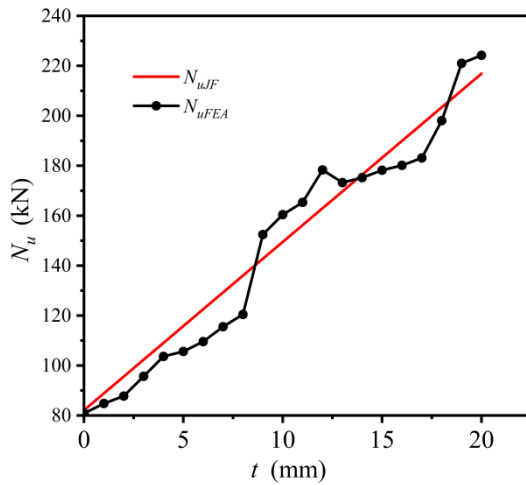
Fig. 17 Comparison of tensile bearing capacity calculated by finite element simulation and Eq.9

Fig. 18 Diagram of the Calculation Results for Eq.5 and Eq.9

Based on Fig. 17, assuming that the connecting pipe did not yield, the key findings are summarized as follows:

(1) The tensile-bearing capacity of the connectors increases with an increase in the baseplate thickness due to an increase in the moment of inertia (I_z) of the composite section formed by the baseplate and angle steel frame.

(2) The tensile-bearing capacities calculated using Eq. 9 show good agreement with those obtained from numerical simulations, suggesting that the tensile-bearing capacity of the connectors under buckling deformation of the angle steel frame can be accurately determined using Eq. 9.

(3) The tensile-bearing capacity of the connectors exhibits a linear relationship with the baseplate thickness, with a slope of 6.74 kN/mm. This implies that for every 1-mm increase in the baseplate thickness, the tensile-bearing capacity of the connectors increased by 6.74 kN.

5.7. Synergistic effect of the connecting pipe and baseplate thicknesses

The individual effects of the connecting pipe and baseplate thicknesses on the tensile-bearing capacity of the connectors were examined in the previous sections. The tensile-bearing capacities of the connectors under two distinct failure modes can be determined using Eq. 5 and Eq. 9. In practical applications, both the connecting pipe and baseplate thicknesses collectively influence the tensile-bearing capacity of the connectors. To ensure that neither the connecting pipe nor the angle steel frame experiences failure, it is advisable to select the lower value of the tensile-bearing capacities obtained using Eq. 5 and Eq. 9. The tensile-bearing capacities of the connectors were obtained using Eq. 5 and Eq. 9, when t = 0, 9, and 14mm, respectively, as shown in Fig. 18.

Based on Fig. 18, the key findings are summarized as follows:

(1) the tensile-bearing capacity curves obtained using Eq. 5 and Eq. 9 intersected at a particular point. On the left side of this intersection point, the tensile-bearing capacity of the connectors is determined by the bulging deformation at the opening of the connecting pipe, which is proportional to the square of the connecting pipe thickness. On the right side of this intersection point, the tensile-bearing capacity of the connectors is determined by the buckling deformation of the angle steel frame, which is independent of the connecting pipe thickness.

(2) when t = 0 mm, the tensile-bearing capacity at the intersection point of the two curves is associated with a connecting pipe thickness of 8 mm (d = 8 mm). On the left side of the intersection point, increasing the connecting pipe thickness could augment the tensile-bearing capacity of the connectors. On the right side of the intersection point, the tensile-bearing capacity of the connectors is governed by the buckling deformation of the angle steel frame and can be calculated using Eq.9, yielding a constant value. It is worth noting that increasing the connecting pipe thickness does not enhance the tensile-bearing capacity of this connector.

(3) The tensile-bearing capacity of connectors shows a significant increasing trend with the increase of d, but its maximum value is significantly regulated by t. When t = 0mm and d < 9mm, the tensile-bearing capacity of connectors increases with d to approximately 80 kN. After that, with the increase of d, the bearing capacity no longer increases. By analogy, when t = 14mm and d < 15mm, the tensile-bearing capacity of connectors increases with d to approximately 175kN. After that, with the increase of d, the bearing capacity no longer increases. The increase of t will significantly enhance the
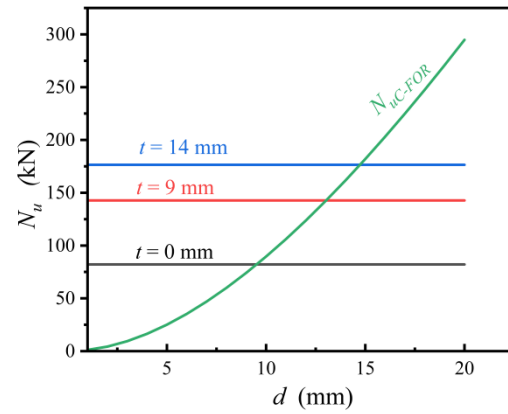
positive contribution of d to the tensile-bearing capacity of connectors. There is a synergistic effect between d and t, jointly determining the tensile-bearing capacity of connectors. In practical applications, the smaller of the two is taken.

6. Conclusions

In this study, the tensile-bearing capacity of an innovative connector designed for OFPV platforms is investigated. First, 18 test specimens were designed and fabricated for tensile tests, which yielded the mechanical behavior of the test specimens including the failure modes, load–displacement curves, and load–strain curves. Second, a finite element model was developed and a comprehensive parametric study was conducted. Finally, the tensile mechanism and loading conditions of the connectors were thoroughly analyzed, and equations were derived to determine the tensile-bearing capacity of the connectors under two distinct failure modes. In addition, the tensile-bearing capacities of the connectors determined using the derived equations were compared with those predicted by the finite element model. The conclusions drawn based on the key findings of this study are as follows.

(1) The failure modes of the connectors are primarily categorized into two distinct modes: bulging deformation at the opening of the connecting pipe and buckling deformation of the angle steel frame.

(2) By performing a comprehensive analysis of the stress conditions and deformation mechanisms of the connectors, equations are derived to calculate the tensile-bearing capacity of the connectors under two distinct failure modes. It is advisable to use the smaller value of the tensile-bearing capacities calculated using the derived equations in practical applications.

(3) The thicknesses of the connecting pipe and baseplate have a pronounced effect on the tensile-bearing capacity of the connectors. The combined effect of these parameters is critical to the overall tensile-bearing capacity of the connectors. In cases where bulging deformation occurred at the opening of the connecting pipe, the tensile-bearing capacity is proportional to the square of the connecting pipe thickness. In cases where buckling deformation occurred on the angle steel frame, the tensile-bearing capacity is directly proportional to the baseplate thickness.

(4) For a constant baseplate thickness, the tensile-bearing capacity curves determined using Eq. 5 and Eq. 9 intersect at a particular point. On the left side of the intersection point, the tensile-bearing capacity of the connectors is predominantly determined by the connecting pipe thickness, which can effectively enhance the tensile-bearing capacity of the connectors. On the right side of the intersection point, the tensile-bearing capacity of the connectors is controlled by the buckling deformation of the angle steel frame, and increasing the connecting pipe thickness does not improve the tensile-bearing capacity of the connectors. However, increasing the baseplate thickness could significantly improve the tensile-bearing capacity of the connectors in this case.

(5) The tensile-bearing capacity of connectors shows a significant increasing trend with the increase of the connecting pipe thickness, but its maximum value is significantly regulated by the baseplate thickness. The increase in the baseplate thickness will significantly enhance the positive contribution of the connecting pipe thickness to the tensile-bearing capacity of connectors. There is a synergistic effect between the thickness of the connecting pipe and the baseplate, jointly determining the tensile-bearing

capacity of connectors. In practical applications, the smaller of the two is taken.

Acknowledgements

References

[1] Trapani, K. and D.L. Millar, "The thin film flexible floating PV (T3F-PV) array: The concept and development of the prototype.", Renewable Energy, 2014. 71: p. 43-50.

[2] Kjeldstad, Torunn, Lindholm, Dag Marstein, Erik Selj and Josefine, "Cooling of floating photovoltaics and the importance of water temperature.", Solar Energy, 2021. 218: p. 544-551.

[3] Shi. W., Yan, C. J., Ren, Z. R., Yuan, Z. M., Liu, Y. Y., Zheng, S. M., Li, X. and Han, X., "Review on the development of marine floating photovoltaic systems.", Ocean Engineering, 2023. 286: p. 115560.

[4] Sahu, A., N. Yadav and K. Sudhakar, "Floating photovoltaic power plant: A review.", Renewable and Sustainable Energy Reviews, 2016. 66: p. 815-824.

[5] Cazzaniga, R., Cicu, M., Rosa-Clot, M., Rosa-Clot, P., Tina, G. M. and Ventura, C., "Floating photovoltaic plants: Performance analysis and design solutions.", Renewable and Sustainable Energy Reviews, 2018. 81: p. 1730-1741.

[6] Lv, S., Lu, M., Liu, W. Z., Li, X. L., Lv, W. H., Liu, Z., Dong, X. C., Lu, T. H. and Yang, B. W., "Recent advances in longitudinal spatial area marine photovoltaics.", Renewable and Sustainable Energy Reviews, 2025. 208: p. 115036.

[7] Garrod, A., Neda Hussain, S., Ghosh, A., Nahata, S., Wynne, C. and Paver, S., "An assessment of floating photovoltaic systems and energy storage methods: A comprehensive review.", Results in Engineering, 2024. 21: p. 101940.

[8] Ghosh, A., "A comprehensive review of water based PV: Flotavoltaics, under water, offshore & canal top." Ocean Engineering, 2023. 281: p. 115044.

[9] Djalab, A., Djalab, Z., El Hammoumi, A., Tina, G. M., Motahhir, S., and Laouid, A. A. "A comprehensive Review of Floating Photovoltaic Systems: Tech Advances, Marine Environmental Influences on Offshore PV Systems, and Economic Feasibility Analysis." Solar Energy, 2024. 277: p. 112711.

[10] Fan, S., Ma, Z., Liu, T., Zheng, C., and Wang, H., "Innovations and development trends in offshore floating photovoltaic systems: A comprehensive review." Energy Reports, 2025. 13: p. 1950-1958.

[11] Yang, Y., Wang, H., Sun, J., Lu, W., & Shao, L., "Research on multi-body towing performance of a novel star-type floating photovoltaic structure." Ocean Engineering, 2025. 333: p. 121509.

[12] Dai, J., Zhang, C., Lim, H. V., Ang, K. K., Qian, X., Wong, J. L. H. and Wang, C. L., "Design and construction of floating modular photovoltaic system for water reservoirs." Energy, 2020. 191: p. 116549.

[13] Chandrasekaran, S., S.A. Uddin and M. Wahab, "Dynamic Analysis of Semi-submersible Under the Postulated Failure of Restraining System with Buoy." International Journal of Steel Structures, 2021. 21(1): p. 118-131.

[14] Li, Z., D. Chen and X. Feng, "Hydroelastic and expansibility analysis of a modular floating photovoltaic system with multi-directional hinge connections." Ocean Engineering, 2023. 289: p. 116218.

[15] Song, J., Kim, J., Chung, W. C., Jung, D., Kang, Y. J. and Kim, S., "Wave-induced structural response analysis of the supporting frames for multiconnected offshore floating photovoltaic units installed in the inner harbor." Ocean Engineering, 2023. 271: p. 113812.

[16] Yan, C., Shi, W., Han, X., Li, X., and Verma, A. S., "Assessing the dynamic behavior of multiconnected offshore floating photovoltaic systems under combined wave-wind loads: A comprehensive numerical analysis." Sustainable Horizons, 2023. 8: p. 100072.

[17] Luo, W., Zhang, X., Tian, X., Cheng, Z., Wen, B., Li, X. and Luo, Y., "Conceptual design and model test of a pontoon-truss type offshore floating photovoltaic system with soft connection." Ocean Engineering, 2024. 309: p. 118518.

[18] Jiang, Z., Dai, J., Saettone, S., Torå, G., He, Z., Bashir, M. and Souto-Iglesias, A., "Design and model test of a soft-connected lattice-structured floating solar photovoltaic concept for harsh offshore conditions." Marine Structures, 2023. 90: p. 103426.

[19] Wang, B., Li, Y., Huang, L., Yao, Y. and Qin, Y., "Dynamic analysis of a novel star-type floating photovoltaic system with flexible connectors." Ocean Engineering, 2024. 304: p. 117854.

[20] Pringle, A.M., R.M. Handler and J.M. Pearce, "Aquavoltaics: Synergies for dual use of water area for solar photovoltaic electricity generation and aquaculture." Renewable and Sustainable Energy Reviews, 2017. 80: p. 572-584.

[21] Wang, Y. D., Zhang, Z. Y., Jiang, L. Z., Zeng, L. J. and Liu, J., "Mechanical Properties of Weather-Resistant Steel Beam-to-Column Connections." Advanced Steel Construction, 2024. 20(3): p.253-265.

[22] Ma, H. H., Ma, Y. Y., Fan, F. and Zhang, Y. N., "Seismic performance of single-layer spherical reticulated shells considering joint stiffness and bearing capacity." Advanced Steel Construction, 2022. 18(02): p. 604-616.

[23] Wang, Z. Q., Zheng, Z., MengXiang, J. W. and Jiang, W. Q., "Inversion Method of Uncertain Parameters For Truss Structures Based on Graph Neural Networks." Advanced Steel Construction, 2023. 19(4): p. 366-374.

[24] Jin, C., F.P. Bakti and M. Kim, "Multi-floater-mooring coupled time-domain hydro-elastic analysis in regular and irregular waves." Applied Ocean Research, 2020. 101: p. 102276.

[25] Chen, M., Guo, H., Wang, R., Tao, R. and Cheng, N., "Effects of Gap Resonance on the Hydrodynamics and Dynamics of a Multi-Module Floating System with Narrow Gaps." Journal of Marine Science and Engineering. 2021. 9(11): p. 1256.

[26] Zou, M., Chen, M., Zhu, L., Li, L. and Zhao, W., "A constant parameter time domain model for dynamic modelling of multi-body system with strong hydrodynamic interactions." Ocean Engineering, 2023. 268: p. 113376.

[27] Chen, M., Ouyang, M., Guo, H., and Zhang, C., "A Coupled Hydrodynamic-Structural Model for Flexible Interconnected Multiple Floating Bodies." Journal of Marine Science and Engineering. 2023.11(4): p. 813.

[28] Chen, M., Zou, M., Zhu, L., Ouyang, M., Liang, Q. and Zhao, W., "A fully coupled time domain model capturing nonlinear dynamics of float-over deck installation." Ocean Engineering, 2024. 293: p. 116721.

[29] Du, J., Zhang, D., Zhang, Y., Xu, K., Chang, A. and Zhao, S., "Design and comparative analysis of alternative mooring systems for offshore floating photovoltaics arrays in ultra-shallow water with significant tidal range." Ocean Engineering, 2024. 302: p. 117649.

[30] Yu, J., Cheng, X., Xie, C., Lu, Z., Ding, A., Wang, X. and Zhao,, "Hydrodynamic analysis of three-module semi-submersible platform and its mooring design." Ocean Engineering, 2024. 310: p. 118576.

[31] Zhang, C., Dai, J., Ang, K. K. and Lim, H. V., "Development of compliant modular floating photovoltaic farm for coastal conditions." Renewable and Sustainable Energy Reviews, 2024. 190: p. 114084.

[32] Mashrah, W., Chen, Z. H., Liu, H. B. and Amer, M. A., "Experimental, numerical, and theoretical study on static behaviour of novel steel dovetail joint subjected to axial tensile load." Advanced Steel Construction, 2022. 18(12): p. 453-464.

[33] Si, Q., Ding, Y., Zong, L. and Liu, H., "Mechanical properties and simulation method of structural steel after high cycle fatigue damage." Advanced Steel Construction, 2023. 200(300): p. 400.

[34] Zhang, Z. W., Li, D., Wang, H. J., Qian, H. L., Fang, W. Q., Jing, X. F. and Fan, F. , "Study of mechanical properties of a novel column-beam-column prefabricated steel frame joint." Advanced Steel Construction, 2024. 20(4): p. 0-344.

[35] ISO 6892-1 Metallic materials-Tensile testing-Part1:Method of test at room temperature, 2019.

[36] Li, B. Q. and Zhang, J. L., "Nonlinear Analysis and Design of Surface Waterproof Polyurea Coating with Consideration of Multiple Effects." Journal of Hydraulic Engineering, 2024, 55(04): p. 437-448.